A brightening of Jupiter's auroral 7.80-μm CH_4 emission during a solar-wind compression

J. A. Sinclair[1], G. S. Orton[1], J. Fernandes[1,2], Y. Kasaba[3], T. M. Sato[4], T. Fujiyoshi[5], C. Tao[6], M. F. Vogt[7], D. Grodent[8], B. Bonfond[8], J. I. Moses[9], T. K. Greathouse[10], W. Dunn[11], R. S. Giles[1], F. Tabataba-Vakili[1], L. N. Fletcher[12], P. G. J. Irwin[13]

[1]*MS 183-601, Jet Propulsion Laboratory/California Institute of Technology, 4800 Oak Grove Dr, Pasadena, CA 91109, United States.*

[2]*Department of Physics and Astronomy, California State University Long Beach,1250 Bellflower Boulevard, Long Beach, CA 90840, United States.*

[3]*Planetary Plasma and Atmospheric Research Center, Tohoku University, Aobaku, Sendai, Miyagi 980-8578, Japan.*

[4]*Space Information Center, Hokkaido Information University, 59-2 Nishinopporo, Ebetsu, Hokkaido 069-0832, Japan.*

[5]*Subaru Telescope, National Astronomical Observatory of Japan, 650 North A'ohoku Place, Hilo, HI 96720, United States.*

[6]*National Institute of Information and Communications Technology, 4-2-1, Nukui-Kitamachi, Koganei, Tokyo 184-8795, Japan.*

[7]*Center for Space Physics, Boston University, 725 Commonwealth Ave., Boston MA 02215, United States.*

[8]*Université de Liège, STAR Institute, Laboratoire de Physique Atmosphérique et Planétaire, Quartier Agora B5c, Allée du Six août 19C, B-4000 Liège, Belgium.*

[9]*Space Science Institute, 4750 Walnut St #205, Boulder, CO 80301, United States.*

[10]*Southwest Research Institute, 6220 Culebra Rd, San Antonio, TX 78238, United States.*

[11]*Department of Space & Climate Physics, University College London, Gower Street, London, WC1E 6BT, United Kingdom.*

[12]*Department of Physics & Astronomy, University of Leicester, University Road, Leicester LE1 7RH, United Kingdom.*

[13]*Atmospheric, Oceanuc & Planetary Physics, Clarendon Laboratory, University of Oxford, Sherrington Road, Oxford OX1 3PU, United Kingdom.*

Enhanced mid-infrared emission from CH_4 and other stratospheric hydrocarbons have been observed coincident with Jupiter's ultraviolet auroral emission[1–3], which demonstrates that auroral processes and the neutral stratosphere of Jupiter are coupled. However, the exact nature of this coupling has remained an open question. Here, we present a time series of Subaru-COMICS images of Jupiter at 7.80 μm measured between January 11-14th, February 4-5th and May 17-20th (UT) 2017, which show both the morphology and magnitude of the auroral CH_4 emission to vary on daily timescales in relation to external solar-wind conditions. The southern auroral CH_4 emission increased in brightness temperature (T_b) by ΔT_b = 3.8 ± 0.9 K between January 11th 15:50 UT - 12th 12:57 UT during a predicted solar-wind compression. During the same compression, the northern auroral emission exhibited a dusk-side brightening, which mimicks the morphology observed in the ultraviolet auroral emission during periods of enhanced solar-wind pressures[4,5]. These results suggest that changes in external solar wind conditions perturb the jovian magnetosphere such that ener-

getic particles are accelerated into the planet's atmosphere, deposit their energy as deep as the neutral stratosphere and modify the thermal structure, abundance of CH_4 or the population of energy states of CH_4. We also find that the northern and southern auroral CH_4 emission evolved independently between the January, February and May images, as has been observed at X-ray wavelengths over shorter timescales[6] and at mid-infrared wavelengths over longer timescales[7].

7.80-μm Subaru-COMICS (Cooled Mid-Infrared Camera and Spectrograph) images were obtained from January 11-14th, February 4-5th and May 17-20th 2017 (UT). A subset of images recorded are shown in Figures 1 and 2, which respectively show southern and northern polar projections at times when the southern auroral region (henceforth 'SAR', between 330-60°W in System III) and northern auroral region (henceforth 'NAR', centred at 180°W in system III longitude) were visible on the disk of Jupiter. These images demonstrate variability of both the magnitude and morphology of the 7.80-μm CH_4 emission over timescales of days to months. Further details of the measurements and processing are provided in the Methods and Supplementary sections.

In terms of the morphology, the strongest 7.80-μm emission in both auroral regions appears enclosed inside the statistical mean of the ultraviolet emissions of the main oval[8]. Figure 3 shows the results of ionosphere-to-magnetosphere mapping model calculations (see Methods) and demonstrates that the positions of strongest CH_4 emission in the auroral regions predominantly correspond to radial distances of >95 R_J (beyond the dayside magnetopause[9] and potentially on open field lines). The exception is the morphology of the emission in the NAR at 16:13 UT on January

12th (Figure 2a), when a poleward, duskside feature of stronger emission parallel to the eastern boundary of the statistical oval was observed. This feature was not present less than 24 hours later (Figure 2b) and we have ruled out variable atmospheric seeing conditions between these two nights as the source of this intermittent morphology (see Supplementary Figure 2). A similar morphology of the ultraviolet auroral emission, described as the 'duskside active region', has also been observed during periods of enhanced solar-wind pressures and has been attributed to duskside/nightside reconnection associated with the Vasyliunas or Dungey cycles or velocity shears caused by changing flows on the nightside magnetospheric flank[4,5,10]. Indeed, ionosphere-magnetosphere mapping calculations map 73°N, 155°W (an example location covered by the duskside feature) to $\sim$100R_J at a local time of 19.0 hr. Unlike the NAR, the SAR does not appear to exhibit any smaller-scale morphology although its position at a comparably higher latitude than the NAR does reduce the effective spatial resolution and the ability to resolve smaller-scale features. In contrast to previous studies[7,11], we find no obvious movement in the longitudinal position of the southern auroral CH_4 emission in the images presented in this work.

In order to quantify temporal changes in the magnitude of the auroral emission and its relation to solar-wind conditions, we calculated the residual radiance between each auroral region and a lower-latitude zonal-mean, henceforth named the auroral-quiescent residual (see Methods). Figure 4 compares the auroral-quiescent residual and uncertainty for both auroral regions and the results of a solar-wind propagation model (see Methods). The solar-wind propagation model predicts the arrival of a solar-wind compression at Jupiter at approximately 22:00 UT on January 11th, when the dynamical pressure was predicted to have increased from $<$0.1 nPa to 0.7 nPa. The auroral-quiescent residual increased from T_b = 8.0 $\pm$ 0.3 K on January 11th 15:50 UT to 11.8 $\pm$ 0.5 K on January 12th 12:57 UT: a net increase of 3.8 $\pm$ 0.6 K in T_b or a $\sim$25% increase in radiance. While the viewing geometries of the SAR differ between these two respective images, forward-model calculations of the 7.80-µm emission (see Methods) at these two geometries differ by only 0.7 K in T_b and thus cannot explain all of the observed change. From January 12th 12:57 UT to January 14th 12:33 UT, the SAR returned to a similar brightness on January 14th as was observed pre-compression and was a similar brightness in all subsequent measurements (although variability intermediate of these measurements cannot be ruled out).

The NAR was not visible on the disk of Jupiter in the images measured on January 11th (before the solar-wind compression) and so we do not know whether it also brightened during the same solar-wind compression. However, the aforementioned duskside-active emission captured by COMICS on January 12th 16:13 UT (Figure 2a) occurred shortly after the solar-wind compression, which reiterates that this morphology is likely driven by enhanced solar-wind conditions and their perturbing effect on the nightside magnetosphere. From January 12th 16:13 UT to January 13th 12:30 UT, the auroral-quiescent residual of the NAR was constant in time within uncertainty and subsequently decreased significantly to 1.2 $\pm$ 1.1 K. Similarly, measurements in May show the NAR emission to be weak and comparable with, if not weaker, than lower-latitude regions. From May 18th to May 19th, there was a marginal increase in the emission in the NAR during a small ($\Delta p_{dyn} \sim$ 0.2 nPa) solar-wind compression however, the change in emission was not significant with respect to measurement uncertainty. Without measurements between the dates of January 13th, February 5th and May 18th, it is uncertain whether the NAR emission was consistently weaker in time or whether it exhibited short-term (daily/weekly) variability and the measurements by chance captured periods of weaker emission. However, we favour the latter possibility given that the February-5th and May-17th measurements were preceded by $\geq$7 days of steady, low pressure ($p_{dyn} < 0.05$ nPa) solar-wind conditions. We note the results of a recent study by Kita et al. 2016[15], which showed the total auroral power during a solar-wind compression exhibited a positive correlation with the duration of steady, quiescent solar-wind conditions preceding the compression. We also note that the northern auroral C_2H_6 emission weakened during periods of low solar activity in previous work, which similarly suggests a connection with solar-wind conditions on longer timescales[13].

The daily variability of the southern auroral CH_4 emission is suggestive the source of the variability occurs in the upper stratosphere/mesophere to thermosphere region (10 - 1 μbar), where the thermal inertial timescales are much shorter ($\sim$4 weeks at 1 μbar[14]) compared to the lower stratosphere ($\sim$30 weeks at 1 mbar[14]). We suggest the observed changes in CH_4 emission result from either: 1) variable auroral-related heating of the 10- to 1-μbar level, 2) auroral-driven changes in the vertical profile of CH_4 near its homopause at $\sim$1 μbar, 3) variable non-LTE effects that modify the population of energy states of CH_4 or 4) some combination of 1-3. In order to explore the first two possibilities and determine what magnitude and type of changes in the vertical profiles of temperature or CH_4 could yield a 7.80-μm ΔT_b = 3 - 4 K increase, we performed a series of radiative-transfer calculations using NEMESIS (see Methods).

As shown in Supplementary Figures 5a-b, assuming the CH_4 abundance is held fixed, a 3

- 4 K change in T_b would require either: 1) the pressure level of the mesosphere-thermosphere transition to move deeper in the atmosphere by approximately a pressure-scale height or 2) the lapse rate in the thermosphere to increase by a factor of 2. The former corresponds to a total, atmospheric temperature increase of more than 100 K at the 0.5-μbar level, assuming a thermospheric lapse rate similar to that measured during Galileo's descent[15], whereas the latter corresponds to a total, atmospheric temperature increase of $\sim$20 K at 0.5 μbar. In steady state, thermospheric general circulation models show that the mesosphere-thermosphere transition pressure is deeper in the auroral regions compared to non-auroral regions[16,17]. Yates et al., 2014[18] performed time-dependent thermospheric circulation modelling to investigate the response of the thermospheric structure and circulation to solar-wind compressions and expansion events. Between steady and compressed solar-wind conditions, the model predicted a $\sim$20-K warming and increase in lapse rate at $\sim$70°N due to increased rates of joule heating at pressures lower than 1 μbar (with the lower model boundary set at 2 μbar). This is consistent with the two-fold increase in thermospheric lapse rate required to brighten the 7.80-μm emission by ΔT_b = 3 - 4 K, as detailed above.

As shown in Supplementary Figure 5c, assuming a fixed vertical temperature profile, increasing the altitude of the CH_4 homopause (with respect to the Moses et al., 2005[20] Model A CH_4 profile) by greater than a pressure-scale height would yield a 3 - 4 K increase in T_b at 7.80-μm. At the 0.2-μbar level, this would correspond to a volume mixing ratio (VMR) increase of $\sim 10^{-4}$. In solving the vertical continuity equation assuming the change in VMR is driven entirely by advection and not a chemical source (i.e. $w = (-\Delta X/\Delta t)/(\Delta X/\Delta z)$, where w is the vertical velocity, X is the VMR, t is time and z is height), a change in vertical wind of 2.7 cm s^{-1} with respect to the steady state would be required. The Bougher et al., 2005 thermospheric model [16] predicts vertical winds at ~70°S of approximately 50 cm s^{-1} at the 0.2-μbar level in steady state and thus a change in vertical wind of 2.7 cm s^{-1} is reasonable. A higher-altitude homopause of CH_4 (and other hydrocarbons) in Jupiter's auroral regions was also found to optimize the consistency between Juno and Hisaki measurements[20].

Non-LTE effects are also likely important at the altitudes where the source of variability has been inferred and/or could itself be the driver of the observed variability. In the absence of a strong radiation source, 'classical' non-LTE effects become non-negligible at pressures lower than 0.1 mbar, where collisional timescales become longer than the spontaneous radiative lifetime[21–23]. Without a sufficient number of thermal collisions, the population of rotational and vibrational energies deviates from the translational energy population and thus can no longer be described as a Boltzmann distribution. In comparison to non-auroral regions, the upper-stratospheric heating present in Jupiter's auroral regions[7,19,25] also yields a larger contribution of photons at mid-infrared wavelengths from pressure levels where classical non-LTE processes become non-negligible. In addition, currents of electrons and ions in Jupiter's auroral regions and the resulting charged-particle collisions and dissociative recombinations may induce a non-Boltzmann population of the excited energy states of CH_4. A further process might be 'H_3^+-shine', where the downward flux of H_3^+ emission in lines in the 3- to 4-μm range 'pump' overlapping CH_4 ν_3 lines, exciting the vibrational modes and thereby modifying the population of lines responsible for the ν_4 band at ~7.80 μm[26]. Modeling of the aforementioned non-LTE processes will be the subject of future work.

We cannot distinguish between temperature, CH_4 abundance, or non-LTE effects in driving the variable CH_4 emission observed between January 11-12th 2017. Nevertheless, either of these processes describes a direct coupling of the neutral stratosphere in Jupiter's auroral regions to the external magnetosphere of Jupiter and solar-wind environment. While daily variability of the northern auroral C_2H_4 and C_2H_6 emission has been observed in previous studies[27,28], we believe the results presented in this work represent a significant advance in understanding of this phenomenon. Firstly, the availability of solar-wind measurements and their modelled propagation to Jupiter's orbit allowed the variability of the CH_4 emission to be tentatively linked to external solar-wind changes and their perturbing effect on the magnetosphere. Secondly, COMICS imaging at high-diffraction limited spatial resolutions have allowed the morphology of the CH_4 emission and its variability to be resolved at finer spatial details and mapped to the outer magnetosphere/magnetopause using ionosphere-to-magnetosphere mapping calculations. Auroral-related heating and chemistry dominate the forcing of the thermal structure and composition at Jupiter's poles [7,19,25] and the results of this paper suggest these processes are directly connected to the external magnetosphere. This phenomenon therefore could be ubiquitous for rapidly-rotating Jupiter-like exoplanets with an internal-plasma source around a magnetically-active star[29]. In particular, MHD (magnetohydrodynamic) simulations of a hot-Jupiter at close orbital separations of 0.05 AU from its host star predict auroral powers of several orders of magnitude larger than on Earth and to affect both polar and equatorial regions[30]. The coupling of the neutral stratosphere and magnetosphere of Jupiter presented in this work may therefore be a process of importance in the near-future characterization of Jupiter-like exoplanets from the James Webb Space Telescope and/or directlyimaged planets whose atmospheres are predominantly sensed at higher latitudes.

1. Caldwell, J., Gillett, F. C. & Tokunaga, A. T. Possible infrared aurorae on Jupiter. *Icarus* **44**, 667–675 (1980).

2. Kim, S. J., Caldwell, J., Rivolo, A. R., Wagener, R. & Orton, G. S. Infrared polar brightening on Jupiter. III - Spectrometry from the Voyager 1 IRIS experiment. *Icarus* **64**, 233–248 (1985).

3. Flasar, F. M. *et al.* An intense stratospheric jet on Jupiter. *Nature* **427**, 132–135 (2004).

4. Grodent, D., Gérard, J.-C., Clarke, J. T., Gladstone, G. R. & Waite, J. H. A possible auroral signature of a magnetotail reconnection process on Jupiter. *J. Geophys. Res.-Space* **109**, A05201 (2004).

5. Nichols, J. D. *et al.* Response of Jupiter's auroras to conditions in the interplanetary medium as measured by the Hubble Space Telescope and Juno. *Geophys. Res. Lett.* **44**, 7643–7652 (2017).

6. Dunn, W. R. *et al.* The independent pulsations of Jupiter's northern and southern X-ray auroras. *Nat. Astr.* **1**, 758–764 (2017).

7. Sinclair, J. A. *et al.* Independent evolution of stratospheric temperatures in Jupiter's northern and southern auroral regions from 2014 to 2016. *Geophys. Res. Lett.* **44**, 5345–5354 (2017b).

8. Bonfond, B. *et al.* The tails of the satellite auroral footprints at Jupiter. *J. Geophys. Res.-Space* **122**, 7985–7996 (2017).

9. Joy, S. P. *et al.* Probabilistic models of the Jovian magnetopause and bow shock locations. *J. Geophys. Res.-Space* **107**, 1309 (2002).

10. Grodent, D. *et al.* Jupiter's Aurora Observed With HST During Juno Orbits 3 to 7. *J. Geophys. Res.-Space* **123**, 3299–3319 (2018).

11. Drossart, P. *et al.* Thermal profiles in the auroral regions of Jupiter. *J. Geophys. Res.* **98**, 18803 (1993).

12. Kita, H. *et al.* Characteristics of solar wind control on Jovian UV auroral activity deciphered by long-term Hisaki EXCEED observations: Evidence of preconditioning of the magnetosphere? *Geophys. Res. Lett.* **43**, 6790–6798 (2016).

13. Kostiuk, T. *et al.* P33C-2155: Variability of Mid-Infrared Aurora on Jupiter: 1979 to 2016. In *American Geophysical Union Fall Meeting 2016. P33C: Juno's Exploration of Jupiter and the Earth-Based Collaborative Campaign III Posters* (2016).

14. Zhang, X. *et al.* Radiative forcing of the stratosphere of Jupiter, Part I: Atmospheric cooling rates from Voyager to Cassini. *Planet. Space Sci.* **88**, 3–25 (2013).

15. Seiff, A. *et al.* Thermal structure of Jupiter's atmosphere near the edge of a 5-μm hot spot in the north equatorial belt. *J. Geophys. Res.* **103**, 22857–22890 (1998).

16. Bougher, S. W., Waite, J. H., Majeed, T. & Gladstone, G. R. Jupiter Thermospheric General Circulation Model (JTGCM): Global structure and dynamics driven by auroral and Joule heating. *J. Geophys. Res.-Planet* **110**, E04008 (2005).

17. Gérard, J.-C. *et al.* Altitude of Saturn's aurora and its implications for the characteristic energy of precipitated electrons. *Geophys. Res. Lett.* **36**, L02202 (2009).

18. Yates, J., Achilleos, N. & Guio, P. Response of the jovian thermosphere to a transient 'pulse' in solar wind pressure. *Planet. Space Sci.* **91**, 27 – 44 (2014).

19. Moses, J. I. *et al.* Photochemistry and diffusion in Jupiter's stratosphere: Constraints from ISO observations and comparisons with other giant planets. *J. Geophys. Res.-Planet* **110**, E08001 (2005).

20. Clark, G. *et al.* Precipitating electron energy flux and characteristic energies in jupiter's main auroral region as measured by juno/jedi. *J. Geophys. Res.-Space* **123**, 7554–7567 (2018). URL `https://agupubs.onlinelibrary.wiley.com/doi/abs/10.1029/2018JA025639`.

21. Appleby, J. F. CH4 nonlocal thermodynamic equilibrium in the atmospheres of the giant planets. *Icarus* **85**, 355–379 (1990).

22. Kim, S. J. Infrared processes in the Jovian auroral zone. *Icarus* **75**, 399–408 (1988).

23. López-Puertas, M. & Taylor, F. *Non-LTE Radiative Transfer in the Atmosphere*. Series on atmospheric, oceanic and planetary physics (World Scientific, 2001). URL `https://books.google.com/books?id=1dC9l0q67SYC`.

24. Sinclair, J. A. *et al.* Jupiter's auroral-related stratospheric heating and chemistry I: analysis of Voyager-IRIS and Cassini-CIRS spectra. *Icarus* **292**, 182–207 (2017a).

25. Sinclair, J. A. *et al.* Jupiter's auroral-related stratospheric heating and chemistry II: analysis of IRTF-TEXES spectra measured in December 2014. *Icarus* **300**, 305–326 (2018).

26. Halthore, R. N., Allen, J. E., Jr. & Decola, P. L. A non-LTE model for the Jovian methane infrared emissions at high spectral resolution. *Astrophys. J. Lett.* **424**, L61–L64 (1994).

27. Kostiuk, T., Romani, P., Espenak, F. & Livengood, T. A. Temperature and abundances in the Jovian auroral stratosphere. 2: Ethylene as a probe of the microbar region. *J. Geophys. Res.* **98**, 18823 (1993).

28. Livengood, T. A., Kostiuk, T. & Espenak, F. Temperature and abundances in the Jovian auroral stratosphere. 1: Ethane as a probe of the millibar region. *J. Geophys. Res.* **98**, 18813 (1993).

29. Nichols, J. D. & Milan, S. E. Stellar wind-magnetosphere interaction at exoplanets: computations of auroral radio powers. *Mon. Not. R. Astron. Soc.* **461**, 2353–2366 (2016). 1606.03997.

30. Cohen, O., Kashyap, V. L., Drake, J. J., Sokolov, I. V. & Gombosi, T. I. The Dynamics of Stellar Coronae Harboring Hot Jupiters. II. A Space Weather Event on a Hot Jupiter. *Astrophys. J.* **738**, 166 (2011). 1102.4125.

Acknowledgements All data presented in this work were obtained at the Subaru Telescope, which is operated by the National Astronomical Observatory of Japan (NAOJ). COMICS observations obtained on January 11, 12 and May 19, 20 were proposed by and awarded to co-author YK using Subaru classical time. COMICS observations on January 13, 14, February 4, 5 and May 17, 18 were proposed by and awarded to co-author GSO through the Keck-Subaru time exchange program. We therefore also acknowledge the W. M. Keck Observatory, which is operated as a scientific partnership among the California Institute of Technology, the University of California and the National Aeronautics and Space Administration and supported by generous financial support of the W. M. Keck Foundation. The authors also wish to recognize and acknowledge the very significant cultural role and reverence that the summit of Maunakea has always had within the indigenous Hawaiian community. We are most fortunate to have the opportunity to conduct observations from this mountain. The research was carried out at the Jet Propulsion Laboratory, California Institute of Technology, under a contract with the National Aeronautics and Space Administration. Many thanks to the NASA Postdoctoral and Caltech programs for funding and supporting Sinclair during this research. Orton was supported by grants from NASA to Jet Propulsion Laboratory/California Institute of Technology.

Author contributions JAS led the analysis of the observations and the preparation of this letter. Co-authors GSO and YK were principal investigators of the awarded telescope time from which the presented data was measured. JAS and co-authors GSO, YK, TMS and TF participated in the measurements at the Subaru telescope. Co-author JF performed the reduction and calibration of the images. Co-authors CT and MFV provided model output, which was invaluable in the interpretation of the results. Co-author PGJI is the lead developer of the NEMESIS code, which was adopted in the paper for radiative transfer forward-model calculations. All remaining authors contributed to the interpretation of the results and the preparation of this publication.

Competing Interests The authors declare that they have no competing financial interests.

Correspondence Correspondence and requests for materials should be addressed to author JAS (email: james.sinclair@jpl.nasa.gov).

Methods

COMICS 7.8-μm images The COMICS (the COoled Mid-Infrared Camera and Spectrograph[1,2]) instrument is mounted at the Cassegrain focus of the Subaru Telescope, which is located at the Mauna Kea Observatory (approximately 4.2 km above sea level). Subaru's 8.2-metre primary aperture provides a diffraction-limited spatial resolution of $\sim$0.24" at 7.8 μm, which corresponds to a latitude-longitude footprint of approximately 2.5° x 2° at ±70° in latitude. COMICS provides both imaging and spectroscopic capabilities over a spectral range of approximately 7 to 25 μm. Images are measured on a 320 x 240 array of Si:As BIB (blocked impurity band) pixels each with a scale of 0.13", which provides a total field-of-view (FOV) of 42" x 32". Images can be measured over a number of discrete filters in both the N band (7 to 13 μm) and Q band (17 to 25 μm). In this work, we focus on images obtained in the 7.8-μm filter, which is sensitive to Jupiter's stratospheric CH_4 emission (Supplementary Figure 3). Images were measured on January 11-14, February 4-5 and May 17-20 2017 (UTC). Measurements were performed during periods when Jupiter was available at airmasses lower than 3. The full disk of Jupiter (with equatorial diameters of $\sim$36" in January, $\sim$39" in February and $\sim$42" in May) could not be measured in a single image by the COMICS field-of-view (FOV). In January and February measurements, the full disk of Jupiter was measured using a 2 x 1 mosaic of individual images centred at Jupiter's mid-northern and mid-southern latitudes. In May, a 2 x 2 mosaic was conducted due to Jupiter's larger size during this time period. For each individual image, A-frames (of Jupiter) and B-frames (dark sky 60" north of Jupiter) were continuously recorded over a total exposure time of 20 seconds. Further details of the measurements presented in this work are provided in Supplementary Table 1.

Imaging processing, calibration and error handling Images were processed and calibrated using the Data Reduction Manager (DRM). A-B subtraction was performed to remove telluric sky emission. The resulting images were then divided by a 'bad pixel mask' accounting for corrupted pixels (due to cosmic ray damage, bright star saturation, manufacturer flaws etc.) and a flatfield in order to remove variations in pixel-to-pixel sensitivity across the detector. A limb-fitting procedure was used to assign latitudes, longitudes and local zenith angles to each pixel on the disk of Jupiter, using the known sub-observer latitude and longitudes at the time of each exposure. The absolute radiometric calibration of the images and correction for telluric absorption was conducted by scaling the observed lower-latitude zonal-mean brightness to those measured by Cassini's CIRS[3] instrument during the 2001 flyby. This procedure is described in greater detail in Fletcher et al., 2009[4]. We chose this method of calibration since experience with past mid-infrared images of Jupiter and Saturn has demonstrated that the radiometric calibration using a standard star provides inconsistency between datasets obtained on different nights[4,5]. As detailed further in the 'Auroral-quiescent residual calculations' section of Methods, our analysis of the images involved comparing the relative brightness of the auroral regions with a lower-latitude region over time, which negates errors introduced by offsets in the absolute calibration between nights. The reduced and radiometrically-calibrated images are shown in Supplementary Figure 1 in units of brightness temperature (T_b) at 7.80 μm. Portions of the image within 6 pixels (or approximately 0.8") of the assigned limb were removed as a conservative means of removing the effects of seeing and diffraction in blurring dark sky together with emission from Jupiter. The noise-equivalent spectral radiance (NESR) was calculated by finding the standard deviation emission of dark-sky pixels more than 1.5" (or approximately 12 pixels) away from the planet. This was calculated for each image to capture changes in sensitivity due to variations in airmass and telluric atmospheric conditions between measurements. A centre-to-limb variation correction in the longitudinal direction was applied to correct for the foreshortening and limb-brightening such that longitudes at different viewing geometries on different nights could be more readily compared. A power-law fit, of the form $\log R = a\log\mu + b$, where R is radiance, $\mu = \cos\theta$ and θ is the zenith emission angle, was performed in each latitude band in order to derive a centre-to-limb correction factor. For January and February measurements, we performed the power-law correction using the January 11th 15:50 UT image (Supplementary Figure 1a) in the northern hemisphere and the January 13th 12:30 UT image (Supplementary Figure 1d) in the southern hemisphere. For May measurements, the May 17th 09:40 UT and May 18 09:35 UT images (Supplementary Figures 1i, j) were similarly chosen to perform the power-law correction in the northern and southern hemispheres, respectively. These specific images were chosen since they best capture non-auroral longitudes in each hemisphere.

Ionosphere to magnetosphere mapping We adopted the magnetosphere-ionosphere mapping calculation by Vogt et al.[6,7] to map a location on the planet in planetocentric latitude and system III longitude to its position in radial distance and local time in the jovian magnetosphere. The calculation is performed by imposing magnetic flux equivalence of a specified region at the equator to the area at which it maps in the ionosphere assuming a given internal field model. For this work, we adopted the VIPAL (Voyager Io Pioneer Anomaly Longitude) internal field model[8] due to its validity in both the northern and southern hemispheres and to larger ($\sim$95 R_J) radial distances. Stepping through latitude and longitude in increments of 1° poleward of ±45° in latitude, the ionosphere-to-magnetosphere mapping calculation was performed to derive the local time and distance within the magnetosphere at each location. Regions enclosed within the statistical ultraviolet oval for which the calculation did not produce a real value were interpreted as mapping beyond the 95 R_J limit of the model, which also marks the estimated position of the dayside magnetopause[9]. This calculation was used to derive the contours of distance shown in Figure 3.

Auroral-quiescent residual calculations Figure 3 demonstrates the areas denoted by ‘Region A’ and ‘Region L’ at both high-northern and high-southern latitudes. Region A (for ‘auroral’) was chosen as a sub-region of the auroral regions that mapped to the outer magnetosphere and was commonly sampled by all measurements presented in Figures 1 and 2. Region L was chosen as a lower latitude region away from the area of auroral influence, which is sampled at $\mu = cos(\theta_{emm})$ (where θ_{emm} is the zenith emission angle on Jupiter) in the range $0.4 < \mu < 1$ in each image. By calculating the residual between Region A and Region L, any inconsistencies in the radiometric calibration from one night to the next are effectively removed, which would otherwise affect a comparison of the absolute radiance in time. The mean radiances within Region A and Region L were calculated. The 1-σ uncertainty on the mean radiance in each region was chosen to be the larger of: 1) the NESR of each image (see Imaging processing, calibration and error handling) scaled by $1/\sqrt{n_p}$ where n_p is the number of pixels averaged or 2) the standard deviation on the mean radiance in the region. The radiances and uncertainties were then converted to brightness-temperature units and the brightness- temperature residual and uncertainty were calculated.

Solar-wind propagation model The Juno spacecraft continues to provide information on the magnetic and charged particle fields whilst performing 53.5-day orbits inside Jupiter’s magnetosphere. However, the Juno spacecraft cannot provide *in-situ* measurements of the external solar-wind conditions outside Jupiter's magnetosphere. In the absence of such measurements, we look instead to modelling results. A solar-wind propagation model[10] was adopted to calculate the solar-wind dynamical pressure ($p_{dyn} = \rho v^2$, where ρ is the density and v is the velocity of the solar wind) impinging on Jupiter's magnetosphere. This model is used extensively by the outer planets magnetosphere community[11–13] in the absence of in-situ measurements of the solar-wind conditions. The model adopts hourly measurements of the solar wind and magnetic field at Earth's bow-shock nose from OMNI[14] as input and then performs 1-D magnetohydrodynamic (MHD) calculations to model the solar-wind flow out to Jupiter's bow-shock. The 1-D model prediction of a 3D problem can introduce uncertainties on the arrival time and magnitude of dynamical pressure of solar wind compressions. When the Earth-Sun-Jupiter angle is less than $\pm 50°$, the uncertainty of the arrival time of the solar wind shock is less than ± 20 h and that of the maximum dynamic pressure is 38%[15]. Given Earth-Sun-Jupiter angles were between 80 - 120° in the January-February 2017 time range, we adopted a 48-hour time error on the solar wind propagation model results. In May 2017, the Earth-Sun-Jupiter angle was approximately 18° and thus we assumed a time error of 20 hours in the May time range. These values also appear commensurate with a statistical comparison of 1-D MHD predictions and solar-wind data measured by several spacecraft[16]. The aforementioned error values are shown in Figure 4 to highlight the potential error to the reader.

Nemesis forward model calculations A single, broadband measurement of the CH_4 emission does not provide sufficient information to invert or *retrieve* atmospheric parameters and determine at what altitudes they vary. Nevertheless, we computed synthetic or 'forward-model' spectra for a range of vertical profiles of temperature and CH_4 in order to explore what changes in those atmospheric parameters could yield the observed, 7.80-μm, ΔT_b = 3 - 4 K brightening of the southern-auroral region. The NEMESIS forward model and retrieval tool[17] was adopted to compute forward-model spectra of the radiance in the COMICS 7.80-μm bandpass. Forward-model spectra were computed using the line-by-line method using the sources of line information for CH_4, CH_3D and $^{13}CH_4$, C_2H_2, C_2H_6, NH_3 and PH_3 detailed in Table 4 of Fletcher et al., 2012[18]. Calculations were performed using a square instrument function with a width of 0.04 cm^{-1} (chosen based on a balance of a sufficiently high spectral resolution to resolve both weak and strong emission lines whilst minimising computational expense) and subsequently convolved with the COMICS 7.80-μm bandpass and the telluric transmission spectrum (see Supplementary Figure 2). The vertical profiles of temperature and CH_4 were varied as detailed below. The remaining parameters of our model atmosphere, including the vertical profiles of C_2H_2, C_2H_4, C_2H_6, NH_3, PH_3, were held constant since they have negligible effect on the spectrum in the 7.80-μm bandpass. Further details of the model atmosphere are provided in Sinclair et al., 2017[19]. It should be noted that the current NEMESIS forward model assumes local thermodynamic equilibrium (LTE) conditions, whereas, conditions in the auroral regions may have departed from LTE as discussed in the main text.

Firstly, we kept the vertical profile of CH_4 and its isotopologues fixed to the 'model A' vertical profile from Moses et al., 2005[20]. Starting from the temperature profile shown in Supplementary Figure 4a, we modified the vertical temperature profile in the 0.1-mbar to 1-μbar range, which includes the transition from the upper stratosphere/mesosphere to the thermosphere. The vertical temperature gradient (or lapse rate) in thermosphere was fixed and the pressure level of the mesosphere/thermosphere transition was varied as shown in Supplementary Figure 5a. For each profile, a forward model was computed at the same viewing angle ($\mu = \cos(\theta_{emm}) = 0.205$, where θ_{emm} is the emission angle) as Region A in the southern auroral region on January 12th 12:57 UT (during the solar-wind compression). The synthetic spectrum was convolved with the 7.80-μm bandpass (as detailed above) and converted into units of brightness temperature (T_b). These T_b values are shown in the legend in Supplementary Figure 5a. A further set of forward models and brightness temperatures were similarly computed, where the pressure level of the mesosphere/thermosphere transition was fixed at 0.2 μbar and the vertical temperature gradient (or lapse rate) was varied, as shown in Supplementary Figure 5b.

Secondly, we fixed the vertical profile of temperature as shown in Supplementary Figure 4a. Starting from the vertical profile of CH_4 derived from model A of Moses et al., 2005[20], the pressure level of the methane homopause was varied as shown in Supplementary Figure 5c, a forward-model radiance in the 7.80-μm bandpass calculated and converted into brightness-temperature units. These values are shown as the legend of Supplementary Figure 5c.

Data & Code availability The COMICS images presented in this work are now publically available on the SMOKA (Subaru Mitaka Okayama-Kiso Archive System, https://smoka.nao.ac.jp/) following an 18-month proprietary period since measurement. Reduced and calibrated images may be requested from author JAS with permission of the principal investigator of the awarded telescope time (see Acknowledgements). The Data Reduction Manager is a suite of IDL software designed for reduction and processing of planetary images and is available in compressed format from co-author GSO upon request (glenn.s.orton@jpl.nasa.gov). The ionosphere-to-magnetosphere mapping calculation is also written in IDL and is available from co-author MFV (mvogt@bu.edu), upon request. Results of the solar wind propagation model in a specific time period may be requested from co-author CT (chihiro.tao@nict.go.jp), upon request. The NEMESIS forward model and retrieval tool is written in Fortran and is available as a GitHub repository: a user account for this repository may be requested from co-author PGJI (patrick.irwin@physics.ox.ac.uk).

1. Kataza, H. *et al.* COMICS: the cooled mid-infrared camera and spectrometer for the Subaru telescope. In Iye, M. & Moorwood, A. F. (eds.) *P. Soc. Photo-Opt. Ins.*, vol. 4008 of *Proceedings of SPIE*, 1144–1152 (2000).

2. Okamoto, Y. K. *et al.* Improved performances and capabilities of the Cooled Mid-Infrared Camera and Spectrometer (COMICS) for the Subaru Telescope. In Iye, M. & Moorwood, A. F. M. (eds.) *P. Soc. Photo-Opt. Ins.*, vol. 4841 of *Proceedings of SPIE*, 169–180 (2003).

3. Flasar, F. M. *et al.* Exploring the saturn system in the thermal infrared: The composite infrared spectrometer. *Space Sci. Rev.* **115**, 169–297 (2004).

4. Fletcher, L. N. *et al.* Retrievals of atmospheric variables on the gas giants from ground-based mid-infrared imaging. *Icarus* **200**, 154–175 (2009).

5. Parrish, P. D. *et al.* Saturn's atmospheric structure: the intercomparison of Cassini/CIRS-derived temperatures with ground-based determinations. In *AAS/Division for Planetary Sciences Meeting Abstracts #37*, vol. 37 of *Bulletin of the American Astronomical Society*, 680 (2005).

6. Vogt, M. F. *et al.* Improved mapping of Jupiter's auroral features to magnetospheric sources. *J. .Geophys. Res.-Space* **116**, A03220 (2011).

7. Vogt, M. F. *et al.* Magnetosphere-ionosphere mapping at Jupiter: Quantifying the effects of using different internal field models. *J. Geophys. Res.-Space* **120**, 2584–2599 (2015).

8. Hess, S. L. G., Bonfond, B., Zarka, P. & Grodent, D. Model of the Jovian magnetic field topology constrained by the Io auroral emissions. *J. Geophys. Res.-Space* **116**, A05217 (2011).

9. Joy, S. P. *et al.* Probabilistic models of the Jovian magnetopause and bow shock locations. *J. Geophys. Res.-Space* **107**, 1309 (2002).

10. Tao, C., Kataoka, R., Fukunishi, H., Takahashi, Y. & Yokoyama, T. Magnetic field variations in the jovian magnetotail induced by solar wind dynamic pressure enhancements. *J. Geophys. Res.-Space* **110** (2005). A11208.

11. Badman, S. V. *et al.* Weakening of Jupiter's main auroral emission during January 2014. *Geophys. Res. Lett.* **43**, 988–997 (2016).

12. Kinrade, J. *et al.* An isolated, bright cusp aurora at Saturn. *J. Geophys. Res.-Space* **122**, 6121–6138 (2017).

13. Lamy, L. *et al.* The aurorae of Uranus past equinox. *J. Geophys. Res.-Space* **122**, 3997–4008 (2017).

14. Thatcher, L. J. & Müller, H.-R. Statistical investigation of hourly OMNI solar wind data. *J. Geophys. Res.-Space* **116**, A12107 (2011).

15. Kita, H. *et al.* Characteristics of solar wind control on Jovian UV auroral activity deciphered by long-term Hisaki EXCEED observations: Evidence of preconditioning of the magnetosphere? *Geophys. Res. Lett.* **43**, 6790–6798 (2016).

16. Zieger, B. & Hansen, K. C. Statistical validation of a solar wind propagation model from 1 to 10 AU. *J. Geophys. Res.-Space* **113**, A08107 (2008).

17. Irwin, P. G. J. *et al.* The NEMESIS planetary atmosphere radiative transfer and retrieval tool. *J. Quant. Spectrosc. RA.* **109**, 1136–1150 (2008).

18. Fletcher, L. N. *et al.* The origin and evolution of saturn's 2011-2012 stratospheric vortex. *Icarus* **221**, 560–586 (2012).

19. Sinclair, J. A. *et al.* Jupiter's auroral-related stratospheric heating and chemistry I: analysis of Voyager-IRIS and Cassini-CIRS spectra. *Icarus* **292**, 182–207 (2017a).

20. Moses, J. I. *et al.* Photochemistry and diffusion in Jupiter's stratosphere: Constraints from ISO observations and comparisons with other giant planets. *J. Geophys. Res.-Planet* **110**, E08001 (2005).

Figure 1 Southern-polar projections of Jupiter's 7.80-μm CH_4 emission. Images were recorded by Subaru-COMICS on (a-c) January 11-14, (d) February 4 and (e-f) May 17, 20 2017. These are a subset of the observations shown in Supplementary Figure 1, when the southern auroral region (330-60°W System III) was fully or partially visible on the disk. Images are shown in brightness temperature units according to the bottom colourbar. Solid, light-blue lines represent the statistical-mean position of the ultraviolet auroral main oval emission[8]. For consistency with the Juno science team and the Earth-based community supporting the Juno mission, increasing System III longitude is shown anti-clockwise.

Figure 2 Northern-polar projections of Jupiter's 7.80-μm CH_4 emission. Images were recorded by Subaru-COMICS on (a-b) January 12-13, (c) February 5 and (d-f) May 18-20 2017. These are a subset of the observations shown in Supplementary Figure 1, when the northern auroral region (centred at 180°W, System III) is fully or partially visible on the disk. Images are shown in brightness temperature units according to the bottom colourbar. Solid, light-blue lines represent the statistical-mean position of the ultraviolet auroral main oval emission[8].

Figure 3 Polar projections and regions chosen for analysis. Subaru-COMICS 7.80-μm images recorded on (a) 2017-01-12 12:57 UT (shown in the south) and (b) 2017-01-13 12:30 UT (shown in the north), as in Figures 1 and 2, shown again here for comparison with the ultraviolet main oval statistical mean[8] and contours that map to difference distances in the external magnetosphere of Jupiter, as indicated in the legend. The region enclosed within the 95 R_J contour is interpreted to map to the outer magnetosphere/magnetopause. Regions A and L are respectively enclosed within the magenta and green regions and were chosen to represent the auroral and non-auroral regions for calculations of the relative radiance and its variability, as detailed in Methods.

Figure 4 Auroral-quiescent residual brightness-temperature values over time. The residual 7.80-μm brightness temperature between Region A (the auroral region) and Region L (a lower-latitude zonal mean) as described in the text/Methods are shown are red points with error bars. Filled points denote results in the south, unfilled points denote results in the north. Results are shown in a) January 2017 and b) May 2017. Predicted solar-wind dynamical pressures at Jupiter (see Methods) are shown as the solid, black line with horizontal error bars showing the potential time error. The Figure suggests a brightening of Jupiter's southern auroral CH_4 emission in response to a solar-wind compression at approximately 22:00 UT on January 11th 2017.

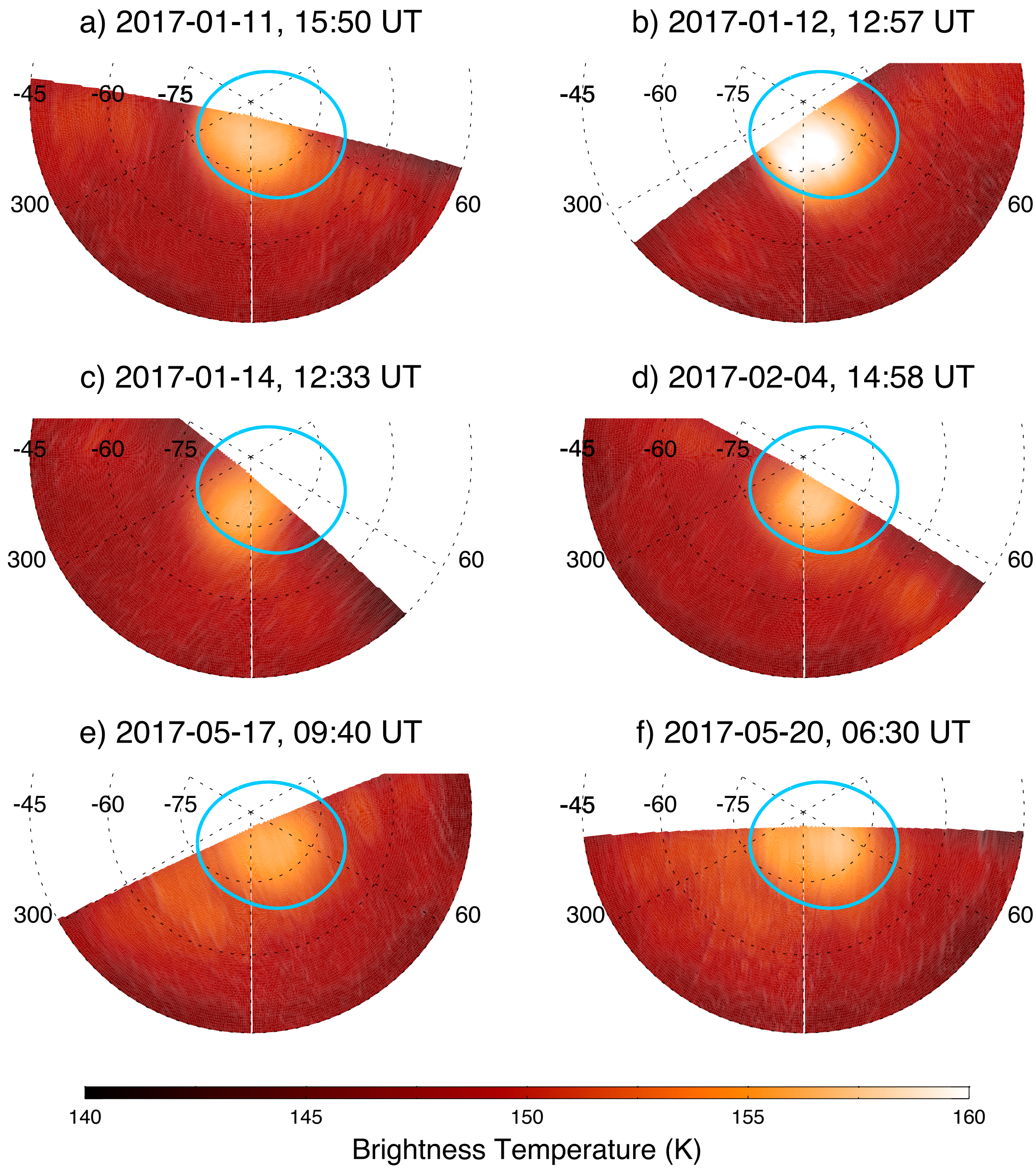
a) 2017-01-11, 15:50 UT
b) 2017-01-12, 12:57 UT
c) 2017-01-14, 12:33 UT
d) 2017-02-04, 14:58 UT
e) 2017-05-17, 09:40 UT
f) 2017-05-20, 06:30 UT
-45
-60
-75
300
60
140
145
150
155
160
Brightness Temperature (K)

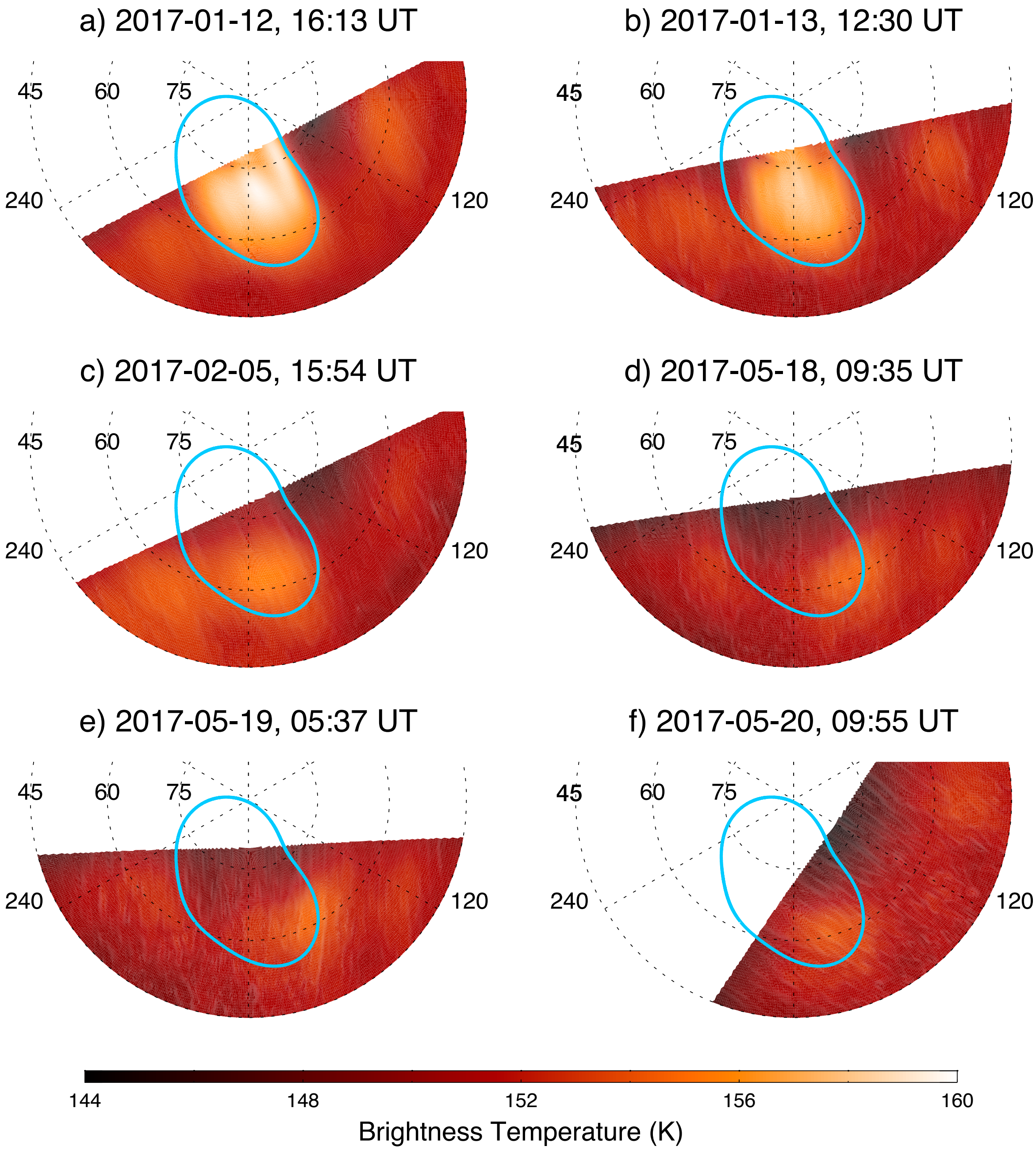
a) 2017-01-12, 16:13 UT
b) 2017-01-13, 12:30 UT
c) 2017-02-05, 15:54 UT
d) 2017-05-18, 09:35 UT
e) 2017-05-19, 05:37 UT
f) 2017-05-20, 09:55 UT
45
60
75
240
120
144
148
152
156
160
Brightness Temperature (K)

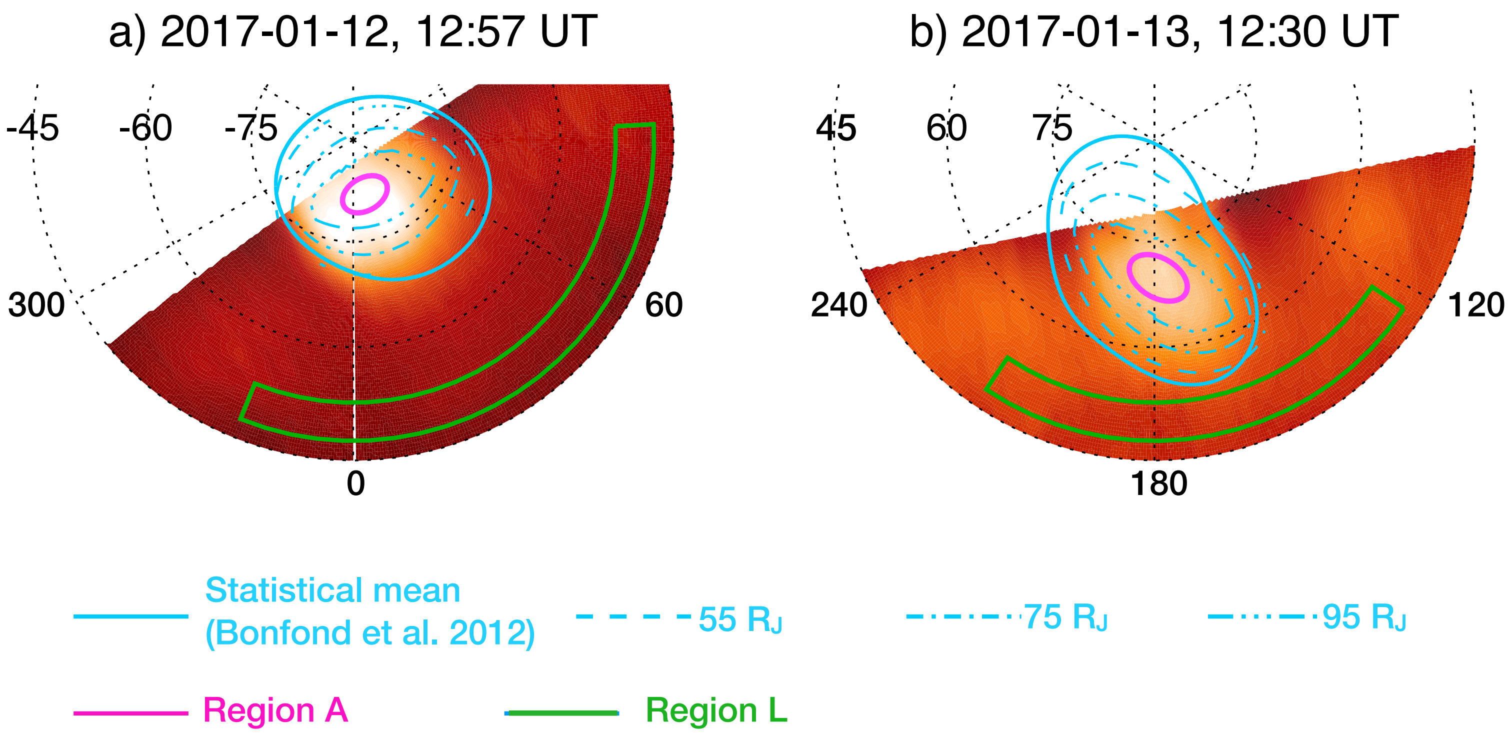

a) 2017-01-12, 12:57 UT
-45
-60
-75
300
60
0
b) 2017-01-13, 12:30 UT
45
60
75
240
120
180
Statistical mean
(Bonfond et al. 2012)
55 R$_J$
75 R$_J$
95 R$_J$
Region A
Region L

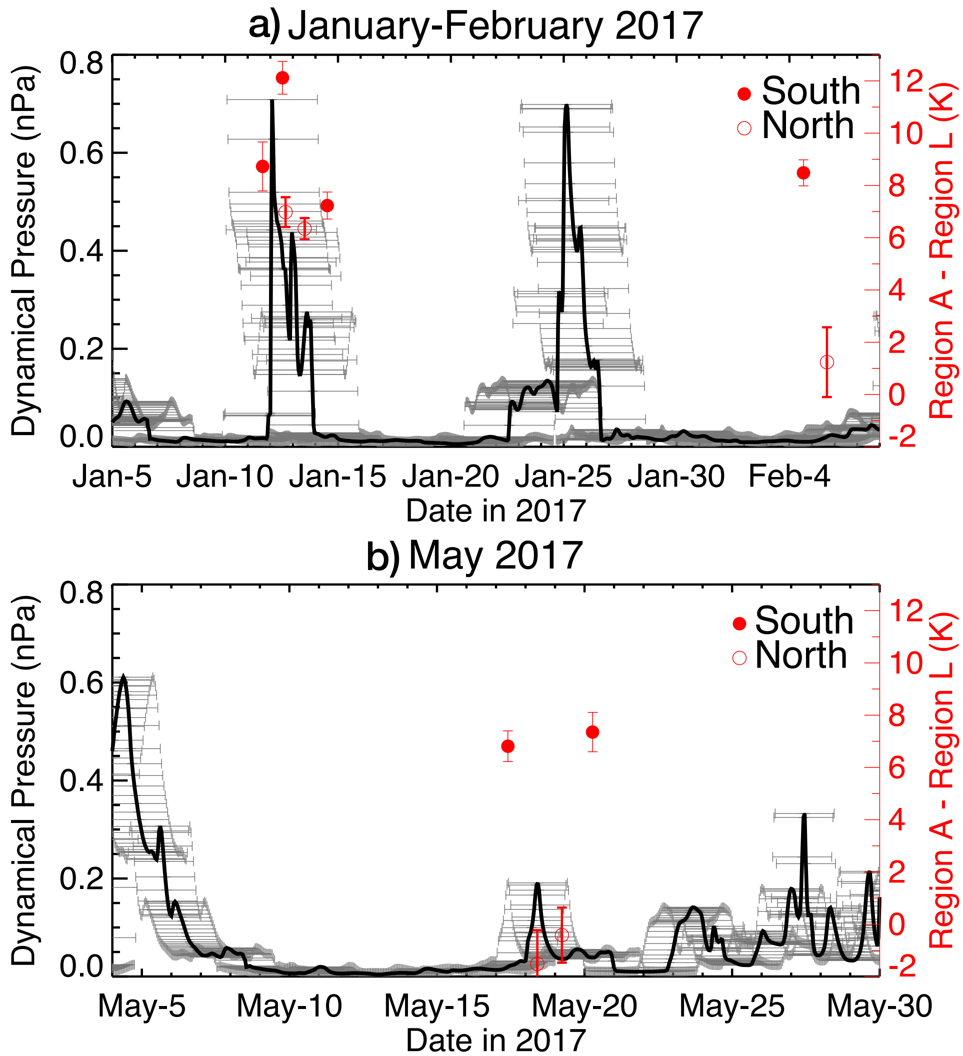

a) January-February 2017
Dynamical Pressure (nPa)
Region A - Region L (K)
South
North
0.0
0.2
0.4
0.6
0.8
-2
0
2
4
6
8
10
12
Jan-5
Jan-10
Jan-15
Jan-20
Jan-25
Jan-30
Feb-4
Date in 2017
b) May 2017
Dynamical Pressure (nPa)
Region A - Region L (K)
South
North
0.0
0.2
0.4
0.6
0.8
-2
0
2
4
6
8
10
12
May-5
May-10
May-15
May-20
May-25
May-30
Date in 2017

Supplementary information to "A brightening of Jupiter's auroral 7.8-μm CH_4 emission during a solar-wind compression" by Sinclair et al. 2019.

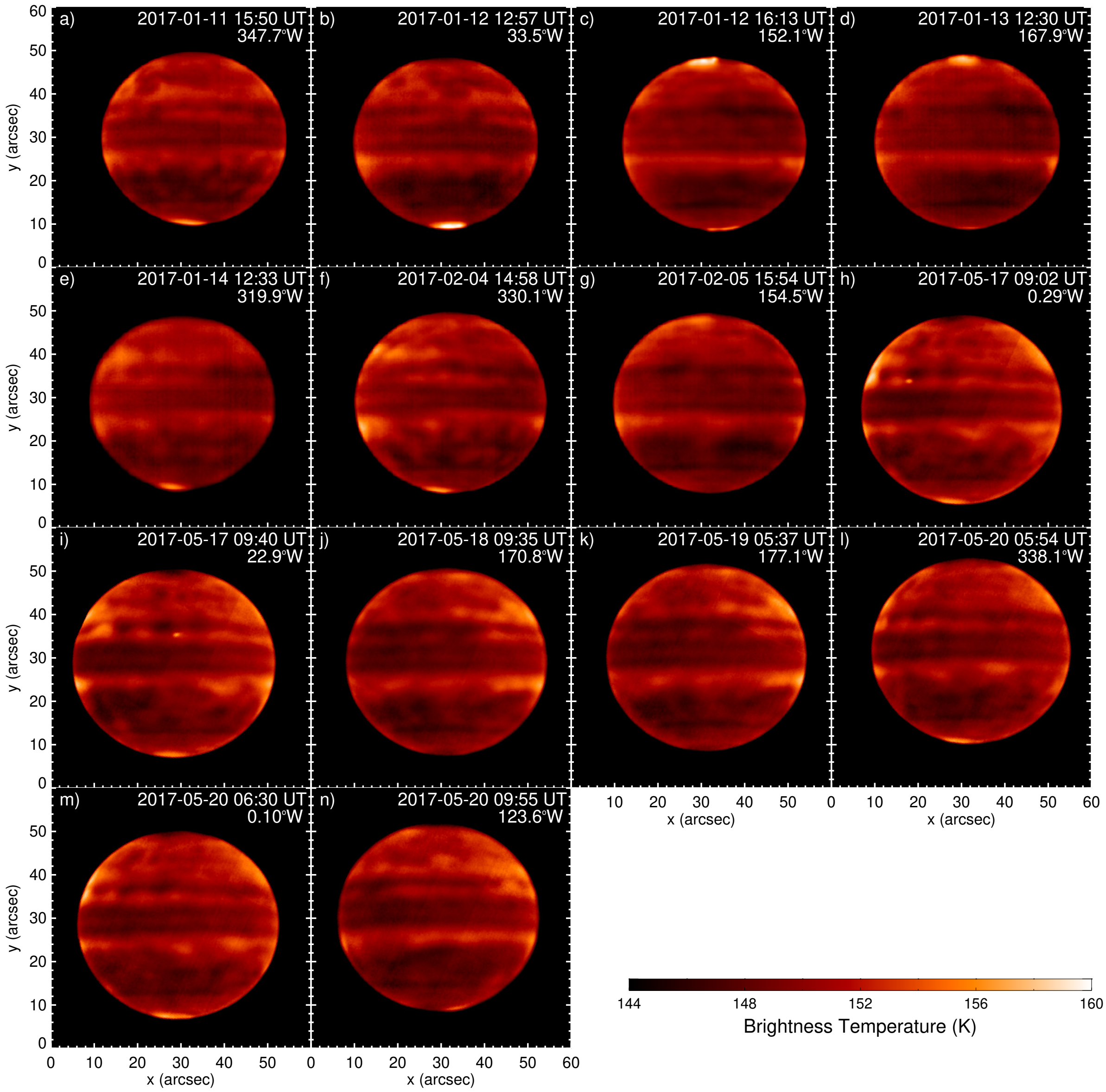

Supplementary Figure 1: Subaru-COMICS images of Jupiter's CH_4 emission. Images are given in chronological order from left-to-right, top-to-bottom and the mean date/time (UTC) and sub-observer System III longitude of each observation are indicated. All images are shown in 7.80-μm brightness-temperature units according to the colourbar at the bottom-right. The bright spot on the disk of Jupiter in panels h) and i) was a Galilean satellite.

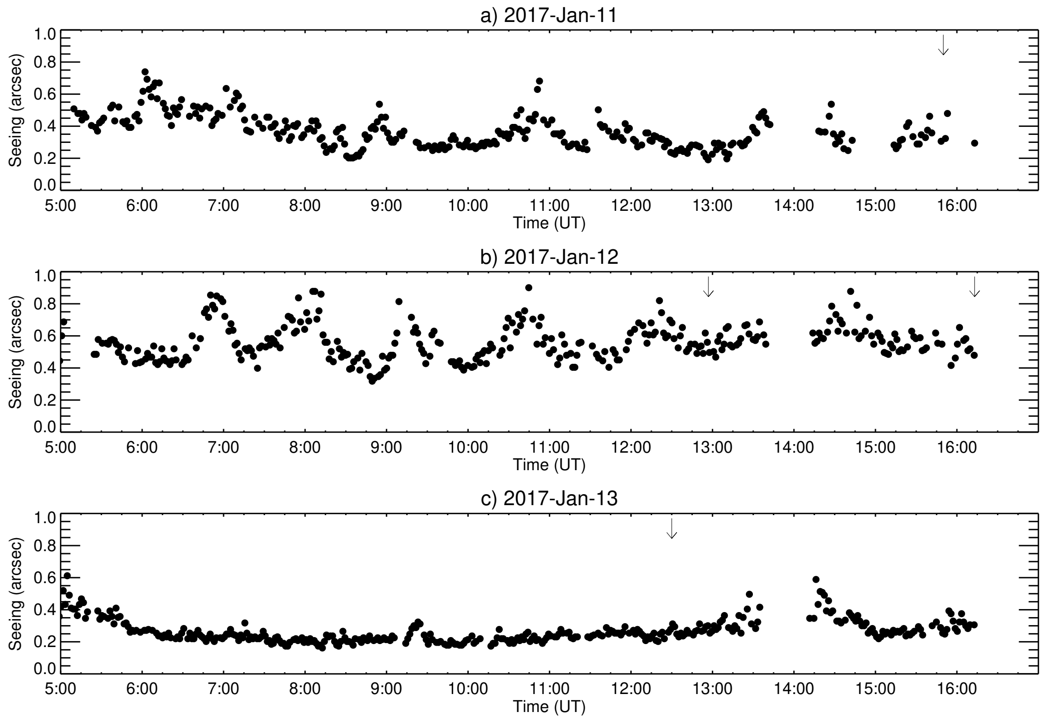

Supplementary Figure 2: Mauna Kea seeing values from January 11-13th. The angular magnitude of seeing (arcsec) at 7.8 μm on a) January 11th (UTC), b) January 12th and c) January 13th 2017. The angular magnitude was measured by the Differential Image Motion Monitor (DIMM) taken from the Mauna Kea weather center (mkwc.ifa.hawaii.edu/current/seeing/) at 0.5 μm and scaled by a factor of $(0.5/7.8)^{0.2}$ for wavelength dependence. Downward arrows mark the times of a subset of COMICS measurements detailed in Supplementary Table 1. These results demonstrate that atmospheric seeing was poorer on January 12th 16:13 UT compared to January 13th at 12:30 UT (∼0.45"). Thus, the finer spatial structure observed in the CH_4 emission on January 12th (Figure 2a, main text) and its absence on January 13th (Figure 2b, main text) cannot be explained by poorer seeing on the latter date.

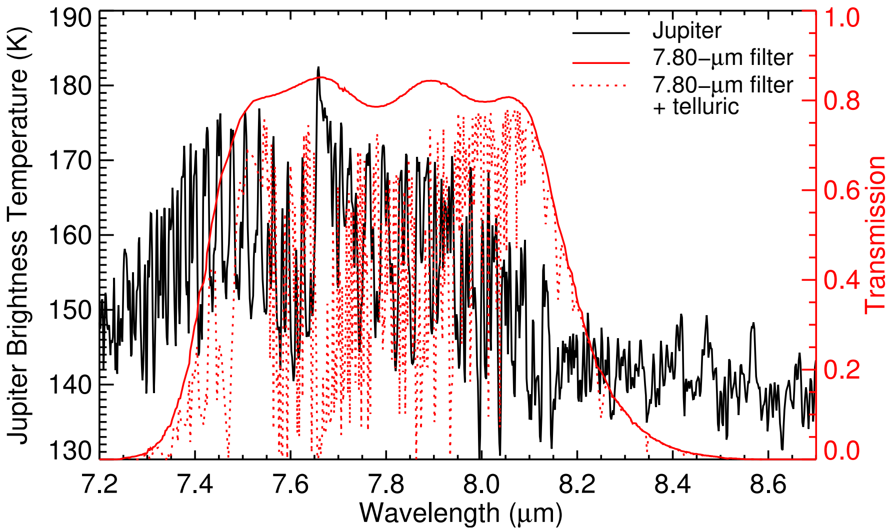

Supplementary Figure 3: The COMICS 7.80-µm bandpass. A brightness temperature spectrum of Jupiter at $\Delta\tilde{\nu} = 0.5\ \mathrm{cm}^{-1}$ (black, solid, of the northern auroral region measured by Cassini-CIRS[1] during the 2001 flyby[2]), the COMICS 7.80-µm filter response (solid, red) including the telluric transmission spectrum (dotted, red) according to the red right-hand axis.

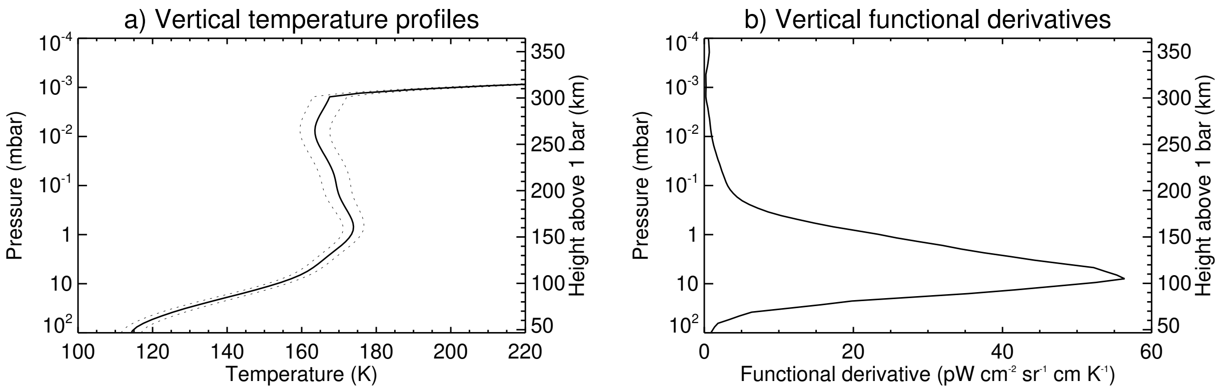

Supplementary Figure 4: Model temperature profile and functional derivatives. Panel (a) shows the vertical temperature profile (solid) and 1-σuncertainty (dotted) retrieved from IRTF-TEXES (Texas Echelon Cross Echelle Spectrograph on NASA's Infrared Telescope Facility[3]) measurements of Jupiter's northern auroral region (centred at 70°W, 180°W) in December 2014[4]. Panel (b) shows the corresponding vertical functional derivatives with respect to temperature (dR_ν/dT_i, where R_ν is radiance at wavenumber, ν and T_i is temperature at the i^{th} pressure level in the atmosphere). This demonstrates that the 7.8-μm bandpass is predominantly sensitive to CH_4 emission in the 20- to 0.5-mbar range with non-zero sensitivity to pressures as low as 0.1 μbar or ∼360 km above the 1-bar level.

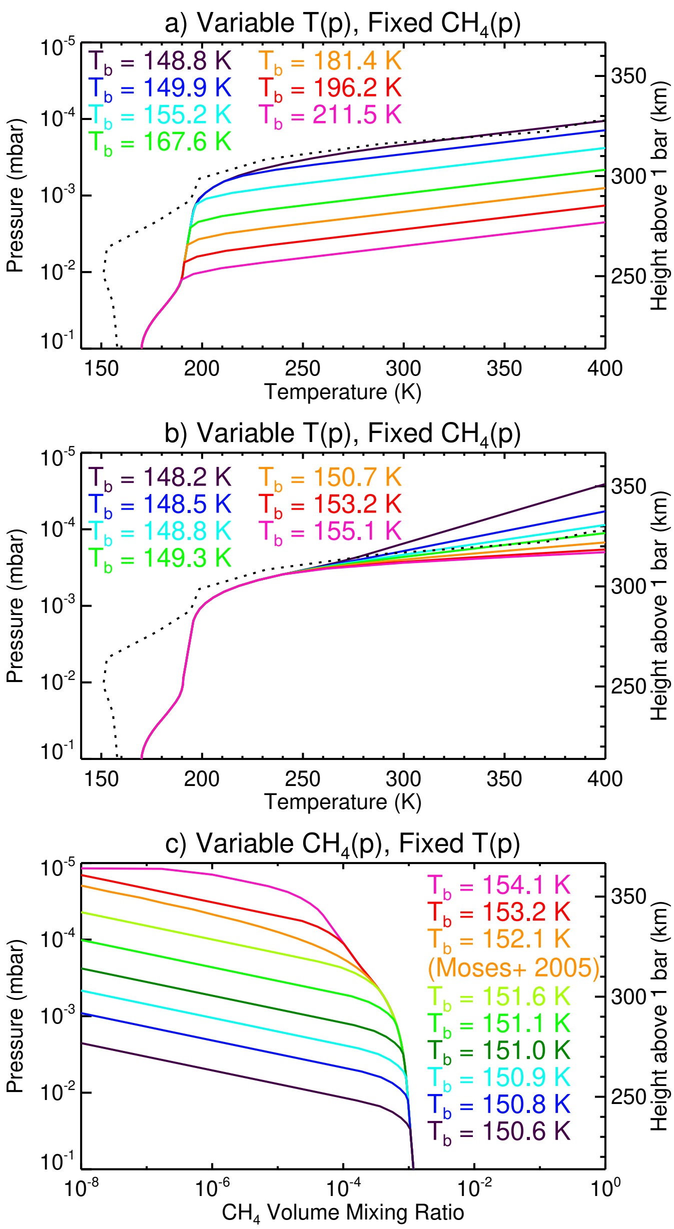

Supplementary Figure 5: Forward-modelled vertical profiles of temperature and CH_4. In panel (a), the vertical profile of CH_4 and the lapse rate in the thermosphere were both fixed while the pressure level of the mesosphere-thermosphere transition was varied as shown. In b), the vertical profile of CH_4 and the transition pressure level were fixed while the lapse rate was modified as shown. In panel (c), the vertical profile of temperature was fixed and the height of the CH_4 homopause was modified as shown. The corresponding forward-modelled brightness temperature (T_b) at 7.80 μm are indicated by the same colour in the legend of each figure. In panels (a) and (b), the temperature profile measured by Galileo during its descent[5] is shown as the dotted, black line for comparison.

Supplementary Table 1: Details of the Subaru-COMICS images adopted in this work. All values represent the mean during the exposure time. Dates/times are given in UTC. Negative relative velocities indicate Jupiter moving towards the Earth.

Date (yyyy-mm-dd)	Time (UTC)	Exposure time (s)	Angular diameter (")	Airmass	Relative velocity (km/s)	Filenames
2017-01-11	15:50	20	36.7	1.14	-28.0	wCOMA00134041
						wCOMA00134043
2017-01-12	12:57	20	36.8	1.79	-28.3	wCOMA00134551
						wCOMA00134553
	16:13	20	36.8	1.13	-28.0	wCOMA00134843
						wCOMA00134845
2017-01-13	12:30	20	36.9	2.09	-28.3	wCOMA00135473
						wCOMA00134475
2017-01-14	12:33	20	37.0	2.00	-28.3	wCOMA00136493
						wCOMA00136495
2017-02-04	14:58	20	39.4	1.13	-25.9	wCOMA00138283
						wCOMA00138285
2017-02-05	15:54	20	39.6	1.18	-25.6	wCOMA00139653
						wCOMA00139655
2017-05-17	09:02	20	42.2	1.18	18.19	wCOMA00139989
						wCOMA00139991
						wCOMA00139993
						wCOMA00139995
2017-05-17	09:40	20	42.2	1.29	18.3	wCOMA00140085
						wCOMA00140087
						wCOMA00140089
						wCOMA00140091
2017-05-18	09:35	20	42.1	1.28	18.3	wCOMA00141011
						wCOMA00141013
						wCOMA00141015
						wCOMA00141017
2017-05-19	05:37	20	42.1	1.24	18.3	wCOMA00141385
						wCOMA00141387
						wCOMA00141389
						wCOMA00141391
2017-05-20	05:54	20	42.0	1.18	18.3	wCOMA00142085
						wCOMA00142087
						wCOMA00142089
						wCOMA00142091
2017-05-20	06:30	20	42.0	1.12	18.3	wCOMA00142181
						wCOMA00142183
						wCOMA00142185
						wCOMA00142187
2017-05-20	09:55	20	41.90	1.40	18.3	wCOMA00142675
						wCOMA00142677
						wCOMA00142679
						wCOMA00142681

References

[1] Kunde, V. G. *et al.* Cassini infrared Fourier spectroscopic investigation. In L. Horn (ed.) *Society of Photo-Optical Instrumentation Engineers (SPIE) Conference Series*, vol. 2803 of *Society of Photo-Optical Instrumentation Engineers (SPIE) Conference Series*, 162–177 (1996).

[2] Sinclair, J. A. *et al.* Jupiter's auroral-related stratospheric heating and chemistry I: analysis of Voyager-IRIS and Cassini-CIRS spectra. *Icarus* **292**, 182–207 (2017a).

[3] Lacy, J. H., Richter, M. J., Greathouse, T. K., Jaffe, D. T. & Zhu, Q. Texes: A sensitive high-resolution grating spectrograph for the mid-infrared. *Publications of the Astronomical Society of the Pacific* **114**, 153–168 (2002). `arXiv:astro-ph/0110521`.

[4] Sinclair, J. A. *et al.* Jupiter's auroral-related stratospheric heating and chemistry II: analysis of IRTF-TEXES spectra measured in December 2014. *Icarus* **300**, 305–326 (2018).

[5] Seiff, A. *et al.* Thermal structure of Jupiter's atmosphere near the edge of a 5-μm hot spot in the north equatorial belt. *J. Geophys. Res.* **103**, 22857–22890 (1998).